Chinese Journal of Catalysis 78 (2025) 279–291

available at www.sciencedirect.com

ScienceDirect

journal homepage: www.sciencedirect.com/journal/chinese-journal-of-catalysis

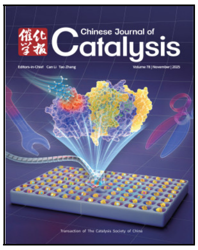

Article

Precursor and dual-template assisted synthesis of highly acidic SAPO-17 molecular sieve: Excellent NH_3-SCR activity of Cu-exchanged forms

Ye Wang [a,b], Pan Gao [c], Dan Zhao [b], Tongrui Liu [b], Sitong Zhou [b], Miao Yang [b,*], Shiping Liu [b], Bing Li [b], Yida Zhou [b], Wenhao Cui [d], Guangjin Hou [c], Peng Tian [b], Zhongmin Liu [b,*]

[a] *College of Chemistry, Zhengzhou University, Zhengzhou 450001, Henan, China*

[b] *National Engineering Research Center of Lower-Carbon Catalysis Technology, Dalian National Laboratory for Clean Energy, Dalian Institute of Chemical Physics, Chinese Academy of Sciences, Dalian 116023, Liaoning, China*

[c] *State Key Laboratory of Catalysis, Dalian National Laboratory for Clean Energy, Dalian Institute of Chemical Physics, Chinese Academy of Sciences, Dalian 116023, Liaoning, China*

[d] *Division of Energy Research Resources, Dalian Institute of Chemical Physics, Chinese Academy of Sciences, Dalian 116023, Liaoning, China*

ARTICLE INFO

Article history:
Received 3 June 2025
Accepted 5 August 2025
Available online 5 November 2025

Keywords:
SAPO molecular sieve
Ammonia selective catalytic reduction
Ultra-wide temperature window
Si distribution
Acidity

ABSTRACT

Silicoaluminophosphate (SAPO) molecular sieves possess diverse architectures and exceptional high-temperature hydrothermal stability, rendering them important acid catalysts. However, enhancing acid concentration of certain SAPO materials remains challenging, which limits their catalytic applications. Here, we report the synthesis of a series of SAPO materials using a developed SAPO precursor plus dual template (SPDT) strategy. A variety of SAPO materials characterized by high silica content and enhanced acidity, such as SAPO-34/56 intergrowths, SAPO-56, and SAPO-17, have been synthesized and thoroughly characterized using various techniques including integrated differential phase-contrast scanning transmission electron microscopy, two-dimensional solid-state nuclear magnetic resonance spectroscopy, and continuous rotation electron diffraction. The use of silica-enriched SAPO precursor combined with the flexible selection of the second template enables the crystalline phase regulation and improves the Si atoms incorporation into the framework. Notably, the synthesized SAPO-17 with abundant Si(4Al) species and unprecedentedly high acid density exhibits exceptional DeNO$_x$ activity after Cu loading, with NO$_x$ conversion exceeding 90% at 175–700 °C. This outstanding performance can be attributed to the unique ERI structure and the increased acidity of SAPO-17. This work not only presents an effective method for synthesizing SAPO molecular sieves with enhanced acidity but also offers a new perspective for expanding the active temperature range of the ammonia selective catalytic reduction reaction.

1. Introduction

Silicoaluminophosphate (SAPO) molecular sieves [1] have received more attention since the industrial application of SAPO-34 catalyst for the methanol-to-olefins (MTO) reaction [2,3]. The small-pore and large-cage structure and moderate

---

* Corresponding author. E-mail: yangmiao@dicp.ac.cn (M. Yang), liuzm@dicp.ac.cn (Z. Liu).

This work was supported by the National Key Research and Development Program of China (2024YFE0207000), the National Natural Science Foundation of China (22171259, 22288101), the Sino-French IRN (International Research Network) and the AI S&T Program of Yulin Branch, Dalian National Laboratory for Clean Energy, CAS (DNL-YL A202206).
https://doi.org/10.1016/S1872-2067(25)64801-7

acidity are the main advantages for SAPO-34, which help realize the high conversion together with high selectivity of ethene plus propene. However, the catalytic application of SAPO materials in high acid concentration required reactions is quite limited due to their insufficient Si incorporation ability. In most cases, the enhanced silica dosage during synthesis leads to impurities or the formation of large area of islands, sacrificing acid concentration [4,5]. Different from aluminosilicate zeolites whose Brønsted acid sites are primarily dependent on the Si/Al ratio and Al atoms distribution, the acidity of SAPO materials is caused by the introduction of Si atoms into $AlPO_4$ framework through single replacement of P (Scheme II, generating Si(4Al) species) or double substitution of neighboring Al and P atoms (Scheme III) forming Si(nAl) (n = 4–0) entities [6–8]. The acid strength caused by different framework Si species has been demonstrated to have an order of Si(1Al) > Si(2Al) > Si(3Al) > Si(4Al) [9–11]. Generally, the acidity of SAPO materials will be weaker than those of zeolites.

The ideal situation for enhancing the acid amount of SAPO materials would be gradually replacing P atoms by Si atoms according to the Scheme II. But generally, the Scheme III densely occurs resulting in large area of Si islands (Si(0Al)) contributing little to acidity. Up to now, DNL-6 with RHO topology represents one of the few highly acidic SAPO materials with a high single Si(4Al) concentration [Si/(Si+Al+P) = 0.182 mol] [12,13]. The presence of a Si−O−Al−O−Si region of DNL-6 significantly enhances its acidity, comparable to that of zeolites [14]. Theoretically, there should be more similar SAPO materials with strong acidity, such as SAPO-17 (ERI) and SAPO-56 (AFX), because both aluminophosphate (AlPO) and aluminosilicate types of ERI and AFX materials have been reported, akin to RHO [15–18]. Confusingly, both SAPO-17 [19–21] and SAPO-56 [22] encounter challenges in concurrently increasing the silica content and optimizing the Si distribution. The advancements in developing novel template agents and seeding methods remain inadequate in surmounting these obstacles, thereby underscoring the urgent need to explore new strategies.

Ammonia selective catalytic reduction of NO_x (NH_3-SCR) as one of the most effective technologies to eliminate NO_x emissions from heavy-duty vehicles is a typical reaction requiring high acid amount. Isolated Cu^{2+} and $[Cu(OH)]^+$ ions are considered as the main active centers of the NH_3-SCR catalysts, which are stabilized by acidic zeolite support [23–25]. The acid density and distribution of zeolites influence the status of loaded Cu ions, their dynamic migration capacity, and consequently catalytic activity and durability of the Cu-based catalysts [26]. It has been recognized that zeolites featuring small 8-ring micropores and double 6-ring (d6r) (or single 6-ring) units are more robust catalyst supports [27–30]. Significantly, small-pore Cu-SSZ-13 has been commercialized as the state-of-the-art NH_3-SCR catalyst [31–34].

In order to better adapt to the complex operating conditions of diesel vehicles and meet the ever-increasing NO_x emission standards [35–37], it is necessary to search for new zeolite candidates to further widen the active temperature window and improve the hydrothermal stability of catalysts. A series of small-pore aluminosilicate zeolites including AEI [38], AFX [39], ERI [40,41], LTA [42,43], UFI [44] and SWY [45] have been explored and their Cu-exchanged forms show potential as alternative NH_3-SCR catalysts. However, to achieve satisfied Si/Al ratios (acidity) for these aluminosilicate zeolites generally requires the aid of complex and expensive organic structural directing agents (OSDAs) and/or the assistance of fluoride media [42,43]. Although some strategies have been developed to synthesize low-silica zeolites with enriched Al pairs without the use of organic amines [46,47], these zeolites require a rigorous multi-step ion exchange process to remove alkali metal cations and reload metal ions. For some special zeolites, such as ERI, the large potassium (K^+) cations lying in small *can* cages cannot be exchanged, resulting in insufficient activity and hydrothermal stability of the catalyst [40]. In contrast, the synthesis of iso-structured high-silica SAPO materials is an alternative and cost-effective approach to obtaining catalyst supports. The ion exchange steps can be reduced [48–50] and some of these materials have shown comparable acidity [14,51,52], better NH_3-SCR activity and high-temperature hydrothermal stability [53,54]. Although the Cu-SAPO-34 has experienced perplexing failure as the commercial NH_3-SCR catalyst, atomic-level investigations show that optimizing the chemical environment of SAPO materials (Si distribution *etc.*) may solve the problem [51,53,55].

In this work, we present an effective SPDT strategy, i.e. using SAPO Precursors and Dual Templates to assist the crystallization of SAPO materials. The crystalline phase is simultaneously regulated by both the SAPO precursor and the dual templates, where SAPO-34/56 intergrowths, SAPO-56 and SAPO-17 with high Si content and abundant Si(4Al) species have been synthesized from the same system, as illustrated in Scheme 1. The materials were well characterized and the crystallization mechanism was also studied. In particular, these materials exhibit significant potential in the NH_3-SCR reaction after Cu loading. The active temperature window of Cu-SAPO-17 spans from 175 to 700 °C, representing the current highest record. Meanwhile, it also has good low/high-temperature hydrothermal stability.

2. Experimental

2.1. Chemicals and materials

All reagents are commercially obtained without further purification. Pseudo-boehmite (Al_2O_3, Shandong Chemical Co., 68.3 wt%), Phosphoric acid (H_3PO_4, Shenyang Federal Chemical Reagent Co., LTD, 80 wt%), Ammonium dihydrogen phosphate ($NH_4H_2PO_4$, Damao Chemical Reagent Factory, 99 wt%), Ammonium chloride (NH_4Cl, Damao Chemical Reagent Factory, 99.5 wt%), Potassium chloride (KCl, Aladdin, 99.5 wt%), N,N,N',N'-tetramethyl-1,6-hexanediamine (TMHDA, $C_{22}H_{48}N_2$, Aladdin, 99.0 wt%), Dimethylamine (DMA, C_2H_7N, Damao Chemical Reagent Factory, 40.0 wt%), Trimethylamine (TMA, C_3H_9N, Aladdin, 30 wt%).

Preparation of amorphous SAPO precursor: The silica

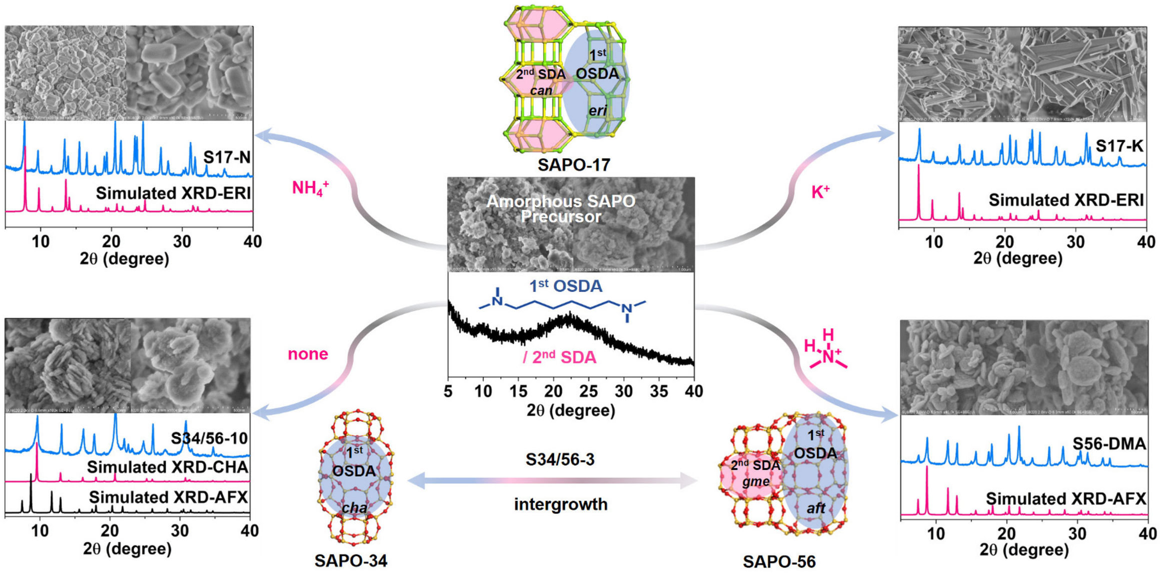

Scheme 1. The SPDT strategy and the synthesized SAPO materials including SAPO-17, SAPO-34/56 intergrowth and SAPO-56.

enriched SAPO materials, including SAPO-34 ($Al_{0.459}Si_{0.199}P_{0.341}O_2$), SAPO-56 ($Al_{0.466}Si_{0.172}P_{0.362}O_2$) and DNL-6 ($Al_{0.471}Si_{0.226}P_{0.303}O_2$), were first synthesized according to references [56-58]. The SAPO materials were calcined at 550 °C for 5 h to remove organic template. The calcined H-type SAPO material was dispersed in a certain amount of water and milled using a planetary ball mill (QM-3SP2, Nanjing, China) with a mixture of agate beads with diameters of 3, 6, and 10 mm. A typical milling condition is 550 rpm for 360 min. After milling, the mud was collected and dried at 110 °C overnight. The collected solid sample was named BM-*X*, where *X* is the type code of SAPO materials. The prepared SAPO precursors in this work included BM-34, BM-56 and BM-D6. Their XRD patterns and SEM images are shown in Figs. S1–S3.

2.2. SPDT synthesis of SAPO materials

2.2.1. A general SPDT method

First, an organic amine template was diluted to a solution with a certain concentration. And then, the organic amine solution and the SAPO precursor were mixed at a certain liquid-solid mass ratio (L/S) in a 50 mL Teflon-lined autoclave. If necessary, a secondary template, additional Al and P sources were added. After thorough stirring, the autoclave was sealed and heated in an oven at 200 °C for several hours. After the reaction, the autoclave was cooled down. The sample was washed with distilled water, centrifuged for recovery, and then dried overnight at 110 °C.

2.2.2. Recipe details of S34/56-L/S

A certain amount of BM-34 was mixed with 10 wt% TMHDA solution with the liquid to solid mass ratios (L/S) of 10 or 3, respectively. The mixture was placed in a 50 mL Teflon-lined autoclave and statically heated in an oven at 200 °C for 24 h.

2.2.3. Recipe details of S56-DMA and S56-TMA

The synthesis conditions were similar to those of S34/56-10, except that a secondary template (the 2nd R), either DMA or TMA, was added. The molar ratio of the 2nd R/TMHDA was 1/5. The mixture was placed in a 50 mL Teflon-lined autoclave and statically heated in an oven at 200 °C for 24 h.

2.2.4. Recipe details of S17-K and S17-N

The synthesis conditions of S17-K and S17-N were also similar to those of S34/56-10. Additional P and Al sources were added with the initial purpose of modification of the composition of S34/56-10. The molar ratio of P_2O_5/Al_2O_3 is 1.0, and the mass ratio of the inorganic oxide (mixture of P and Al sources) to SAPO precursor is 1/7. Initially, $NH_4H_2PO_4$ and Al_2O_3 were used. The product was SAPO-17 unexpectedly which was named S17-N. In order to investigate the role of NH_4^+ ions, $NH_4H_2PO_4$ was replaced by single H_3PO_4, H_3PO_4/NH_4Cl and H_3PO_4/KCl, respectively. S34/56-10 is still the final product when single H_3PO_4 is used. SAPO-17 was the final product when NH_4Cl or KCl is present. The latter was named S17-K. When BM-34 was replaced by BM-D6 or BM-56 while other reaction conditions were kept constant, the SAPO-17 was the final product but always contaminated by other SAPO impurity.

2.3. Characterization

Some conventional characterization details were presented in supplementary materials including the powder X-ray diffraction (PXRD) patterns, scanning electron microscope (SEM), X-ray fluorescence (XRF) spectrometer, thermogravimetric (TG) analyses, N_2 adsorption-desorption isotherms, temperature-programmed desorption (NH_3-TPD), the temperature-programmed reduction of hydrogen (H_2-TPR), electron paramagnetic resonance (EPR) spectrum and the ultraviolet-visible (UV-vis) spectrum and solid-state magic angle spinning nuclear magnetic resonance (MAS NMR) measurements.

The high-resolution transmission electron microscopy (HRTEM) images were obtained on a JEM-F200 transmission electron microscope. Integrated differential phase-contrast scanning transmission electron microscopy (iDPC-STEM) experiments were performed using a Cs-corrected microscope, operated at 300 kV. The convergence semi-angle we used was 9.8 mrad. The probe current was ~1 pA, and the dwell time was 2.5 μs/pixel. The selected area electron diffraction (SAED) patterns for reconstructing continuous rotation electron diffraction (cRED) data were collected on JEOL 2100plus equipped with an ASI camera at 200 kV. The obtained series of SAED patterns were reconstructed by REDp software.

Two-dimensional (2D) solid-state MAS NMR measurements were performed on a wide-bore Bruker Avance III 600 MHz spectrometer (14.1 T) equipped with a 3.2 mm HXY triple resonance MAS NMR probe, with resonance frequencies were 600.13, 156.4 and 242.93 MHz for ^{1}H, ^{27}Al and ^{31}P respectively. 2D ^{27}Al triple quantum magic angle spinning (3Q MAS) NMR spectrum was collected using the three-pulse Z-filter sequence [59]. The triple quantum coherence was excited and converted using rf. field strength of 90 kHz with pulse widths of 6.6 and 2.2 μs, respectively. After a Z-filter period of 20 μs, a central-transition selective π/2 pulse with pulse width of 15 μs was applied prior to the signal acquisition, and the recycle delay was set to 0.5 s. 512 scans were accumulated for each t1 point, and a total of 64 t1 points with increment of 50 μs were collected for the 2D experiments. A shearing transformation was applied to obtain a pure absorption-mode 2D contour plot. The simulation of the lineshape of each signal was performed using the DMFIT software [60], by which the isotropic chemical shift ($\delta_{\rm iso}$) values and quadrupolar product, PQ were extracted. The 2D ^{27}Al-^{31}P triple quantum (3Q) J-coupling refocused insensitive nuclei enhancement by polarization transfer (3Q-J-RINEPT) spectrum was collected using the ^{1}H-^{31}P-^{27}Al triple resonance mode, where the initial 3Q conherence and conversion condition was the same as that in the 3QMAS NMR. The pulse widths of the $\pi/2$ and π pulses for the ^{31}P and ^{27}Al were set to 5.2 μs/10.4 μs and 8.5 μs/17 μs, respectively, and the total delay time of 7.6 ms (1.9 ms × 4) was applied for the J-RINEPT scheme. 9600 scans were accumulated for each t1 points with a recycle delay of 0.05 s, and a total of 32 t1 points with increment of 50 μs were collected for the 2D experiment. The 2D spectrum was obtained via Fourier transformation, and the chemcial shift range of the indrect dimension (^{27}Al, F1) should be adjust according to the 3QMAS experiment to ensure a rational chemical shift scale.

X-ray absorption near-edge structure (XANES) and extended X-ray absorption fine structure (EXAFS) spectra at the Cu K edge were recorded at the P65 beamline of the PETRA III synchrotron (DESY, Hamburg) in transmission mode. The energy of the X-ray photons was selected by a Si(111) double-crystal monochromator and the beam size was set by means of slits to 0.2 (vertical) × 1.5 (horizontal) mm^2. The spectra were normalized and the background of EXAFS was subtracted by using Athena program from the IFEFFIT and Demeter packages [61].

The k^2-weighted EXAFS were Fourier transformed (FT) in the k range of 2.5–12 Å. The $S_0^2 = 0.89$ was obtained by fitting Cu foil reference spectrum and used for further fittings. The interatomic distances (r), energy shift (δE_0), coordination numbers (CN), and mean-square deviation of interatomic distances (σ^2) were refined during the fitting. The absolute misfit between the theory and the experiment is expressed by ρ.

2.4. Catalyst reactions

The NH_3-SCR activity tests were performed in a fixed bed with the gas hourly space velocity (GHSV) of 180000 h^{-1}. A mixture of 300 mg of catalyst (60–80 mesh) and 1900 mg of quartz beads (60–80 mesh) was transferred to a quartz tubular reactor. Prior to testing the activity, the catalyst was heated to 550 °C (2 °C/min) and maintained at this temperature for 30 min in the presence of feed gases. Then, the catalyst was cooled down gradually to 150 °C and started to test. The feed gases were balanced with N_2 and the final component is 500 ppm NO, 500 ppm NH_3, 14% O_2, and 4.5% H_2O. Fourier transform infrared (FTIR) spectrometer (Tensor 27, Bruker) was used to detect NO, NO_2, and N_2O in the inlet and outlet gases.

NO_x conversion (%) = $\{[([NO]_{\rm in} + [NO_2]_{\rm in}) - ([NO]_{\rm out} + [NO_2]_{\rm out}) + N_2O_{\rm out} - N_2O_{\rm in}]/([NO]_{\rm in} + [NO_2]_{\rm in})\} \times 100\%$

N_2 selectivity (%) = $[1 - ([NO_2]_{\rm out} + 2[N_2O]_{\rm out})/([NO_x]_{\rm in} + [NH_3]_{\rm in})] \times 100\%$

High-temperature (HT) hydrothermal aging was carried out at 750 or 800 °C for 16 h in the presence of 12% H_2O in air. Low-temperature (LT) hydrothermal aging was carried out at 80 °C for 24 h in the presence of 12% H_2O in air.

3. Results and discussion

3.1. Synthesis and characterizations of SAPO materials by SPDT method

Typically, amorphous SAPO precursors BM-34, BM-56 and BM-D6 were first prepared by milling the corresponding calcined SAPO-34, SAPO-56 and DNL-6 for 6 h (Figs. S1–S3), respectively, and then the desired precursor was charged into an organic amine solution to hydrothermally recover its crystallinity. BM-34 was the first precursor to be tried. As shown in Table 1 and Fig. S4, the symbiotic phases of SAPO-34 and SAPO-56, named S34/56-L/S (L/S is the mass ratio of the TMHDA solution to the BM-34 precursor) were crystallized in a 10 wt% TMHDA solution at 200 °C for 24 h. The occupancy of the two phases could be regulated by changing L/S value. DIFFaX simulation (Fig. S5) speculates that there is over 90% of SAPO-34 in S34/56-10 and 40% for S34/56-3. iDPC-STEM study confirms the intergrowth of CHA and AFX phases in S34/56-3 (Fig. S6), while S34/56-10 is very likely to be a pure SAPO-34. Notably, pure SAPO-56 can only be obtained when introducing additional small organic amines like DMA and TMA (S56-DMA and S56-TMA in Table 1 and Fig. S7). On the other hand, when a small amount of $NH_4H_2PO_4$ and Al_2O_3 were charged together with BM-34 precursor into the TMHDA solution, pure SAPO-17 could be prepared. Further experiments confirmed that the presence of NH_4^+ or K^+ ions

Table 1

Synthesis conditions and results of SAPO materials[a].

Sample	Mass ratio of L/S[c]	2nd template[d]	Chemical compositions[e]	SSA[f] (m² g⁻¹)			Pore volume[g] (cm³ g⁻¹)		OSDA[h] (wt%)	C/N[j]	Strong acid[m] (mmol g⁻¹)	Cu/Si[e]
				S_{BET}	S_{micro}	S_{ext}	V_{total}	V_{micro}				
S34/56-10	10:1	—	$Al_{0.470}Si_{0.201}P_{0.328}O_2$	558	507	51	0.34	0.25			1.25	
S34/56-3	3:1	—	$Al_{0.455}Si_{0.217}P_{0.327}O_2$	568	506	62	0.34	0.25		4.60	1.14	
S56-DMA	10:1	DMA	$Al_{0.496}Si_{0.193}P_{0.311}O_2$	571	520	51	0.33	0.25	18	4.89	1.17	0.14
S56-TMA	10:1	TMA	$Al_{0.492}Si_{0.197}P_{0.311}O_2$	547	478	69	0.39	0.23				
S17-N[b]	10:1	NH_4^+	$Al_{0.491}Si_{0.197}P_{0.312}O_2$	479	434	45	0.29	0.21	16	3.84	1.06	0.08/0.14/0.22
S17-K[b]	10:1	K^+	$Al_{0.487}Si_{0.196}P_{0.317}O_2$	330	306	24	0.20	0.15	13	5.00	0.59	0.14
S17-C	N/A	N/A	$Al_{0.437}Si_{0.185}P_{0.378}O_2$	448	403	45	0.32	0.20	11.5		0.36	0.12
S56-C	N/A	N/A	$Al_{0.452}Si_{0.204}P_{0.344}O_2$	616	547	70	0.37	0.27				

[a] The reaction condition is 200 °C, 24-48 h. [b] Solid P and Al sources (S_{pAl}) were added with the molar ratio of 1/1 for P_2O_5/Al_2O_3. The mass ratio of S_{pAl}/BM-34 is 1/7. [c] L is the 10 wt% TMHDA solution, S is the BM-34 precursor. [d] The molar ratio of the 2nd template/TMHDA is 1/5. [e] Determined by XRF analysis. [f] SSA (specific surface area) is calculated by the BET method from the N_2 sorption isotherms at 77 K. [g] The micropore volume is determined from the adsorption capacity at P/P_0 = 0.99 and calculated by the t-plot method. [h] Determined by TG analysis. [j] Determined by CHN elemental analysis. [m] Determined by NH_3-TPD.

with the additional P and Al sources is necessary for synthesizing pure SAPO-17, which are named S17-N and S17-K, respectively (Table 1, Figs. 1 and S8). These results suggest that the SAPO crystalline phase can be regulated by using milled amorphous SAPO precursor and the secondary template.

It is noteworthy that all the SAPO products synthesized by SPDT method with an L/S of 10 have high silica contents (~20%) (Table 1). The high normalized molar Al contents above 47% suggest that most of the Si atoms incorporate the framework by replacing P positions obeying the Scheme II mechanism forming Si(4Al) environment [6–8]. Efforts for conventional hydrothermal synthesis of high silica SAPO-17 (S17-C) and SAPO-56 (S56-C) with the assistance of seeds and the secondary template all received unsatisfied results. The crystalline phases were easily contaminated by impurities, and large-area Si islands formed as revealed by solid-state ^{29}Si NMR (Table S1 and Figs. S9–S13). It confirms that SPDT strategy is an effective way to synthesize SAPO materials with enhanced Si content. The high acid concentration of these SAPO products has been subsequently confirmed by NH_3-TPD and solid-state ^{1}H NMR, which will be discussed below.

3.2. Understanding the SPDT method

The roles of SAPO precursor and dual templates were further studied to understand the crystallization mechanism of the SPDT process. Our previous mechanism studies on recrystallization of BM-34 precursor found that BM-34 dissolves and releases Si-O-Al-bonds containing fragments in the early stage of crystallization. It promotes the nucleation, Si incorporation and distribution optimization of SAPO products [62]. Many types of organic amine solutions can restore the crystallinity of BM-34 to SAPO-34, such as morpholine and diethylamine. If other crystalline phases are formed under such a simplified system with BM-34 as the only Si, P and Al sources, it suggests that the template is strongly oriented to non-CHA crystal structures. DFT calculation (Fig. S14) reveals that TMHDA has the lowest interaction energy of –240 kJ mol⁻¹ with the ERI-AlPO4 framework, while those with CHA (–166 KJ mol⁻¹) and AFX (–172 kJ mol⁻¹) are relatively higher and comparable. Therefore, it is believed that the crystallization rates of the CHA-AlPO4 and AFX-AlPO4 are close under the

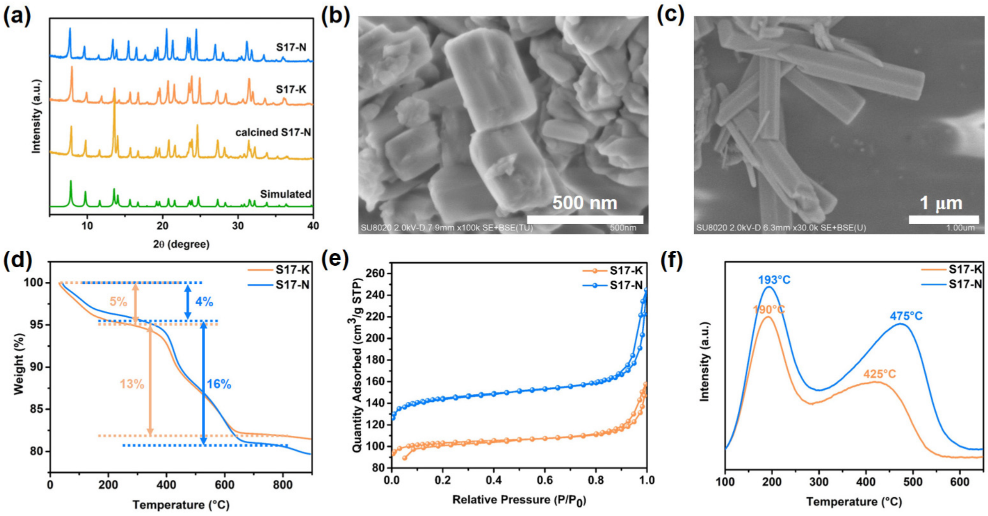

Fig. 1. Simulated and experimental XRD patterns (a), SEM images (b,c), TG analysis (d) of as-synthesized S17-N and S17-K. N_2 adsorption (e) and NH_3-TPD profiles (f) of calcined S17-N and S17-K samples.

guidance of single TMHDA. Meanwhile, the two phases are prone to symbiosis because they have the same connection mode along [001] direction [63,64]. Additional small organic amines, such as DMA and TMA, are suitable to stabilize *gme* cage [22]. Thus, the crystallization rate of AFX accelerates, yielding pure SAPO-56, when DMA or TMA appears as the secondary template. Both K^+ and NH_4^+ ions are suitable to stabilize *can* cage. When the additional Al and P sources are added together with BM-34, the nucleation of AlPO-17 gets faster with the assistance of NH_4^+ or K^+ ions. The crystallization of SAPO-17 is thus promoted which becomes the final product consequently. Intermittent sampling (Figs. S15 and S16) during the crystallization of S17-N revealed that minor SAPO-56 still appears in the early stage of the reaction. SAPO-56 gradually disappears as the prolonged reaction time. It indicates that SAPO-17 is a thermodynamically stable phase under the investigated conditions. The nucleation and crystal growth rates are jointly controlled by the inorganic source and dual templates, where the secondary template plays a great role to modulate the final crystalline phase.

The structural directing ability of the SAPO precursor was also investigated by using amorphous ball-milled SAPO-56 (BM-56) and DNL-6 (BM-D6) instead of BM-34 to synthesize the target SAPO materials. As shown in Fig. S17, pure SAPO-56 with high crystallinity can be synthesized from BM-56 precursor with the assistance of DMA (BM-56-DMA). Using BM-D6 as a precursor receives a mixture of DNL-6 and SAPO-43 with low crystallinity. Attempts to synthesize SAPO-17 always yield SAPO-56 or DNL-6 as an impurity (Fig. S18). The results show that SAPO precursor affects the crystallization greatly through providing structural units and nutrient for nucleation and crystallization. Because of the lack of d6r units for DNL-6, it is more difficult to receive the target AFX and ERI structure even with suitable templates. It is expected to design and synthesize more novel SAPO materials through the selection of precursor and dual templates.

3.3. Structural and acidic characterizations of SAPO-17s

The PXRD patterns of S17-N and S17-K (Fig. 1(a)) show the characteristic peaks attributed to ERI topology, confirming their purity and high crystallinity. S17-N exhibits a uniform hexagonal prism morphology in the submicron range (Fig. 1(b)). While S17-K is rod crystals with a length of over 3 μm, and an aspect ratio of about 10 (Fig. 1(c)). The existence of template TMHDA is confirmed by the solid-state ^{13}C MAS NMR spectrum (Fig. S19). Elemental analyses show average C/N ratios of 3.84 and 5.0 for S17-N and S17-K, respectively (Table 1). Since the C/N ratio of TMHDA is 5, the decreased C/N ratio of S17-N suggests the coexistence of NH_4^+ ions. The total amounts of guest molecules are determined by TG analysis (Fig. 1(d)). The H-form S17-N can be easily obtained by calcining it at 600 °C for 4 h (Fig. 1(a)), and the N_2 sorption isotherms (Fig. 1(e)) show a typical Langmuir type I curve with a BET surface area of 479 $m^2\ g^{-1}$ and micropore volume of 0.21 $cm^3\ g^{-1}$. The relatively low specific surface area and micropore volume of S17-K are due to the occupancy of K^+ ions (Table 1). The NH_3-TPD profiles of S17-N (Fig. 1(f)) present two broad and large desorption peaks centered at 193 and 475 °C, respectively. The latter shows an asymmetric peak shape, suggesting at least two Brønsted acid sites with medium and strong strength. Such a large desorption peak area at high temperature is comparable to those of high silica DNL-6 [14] and aluminosilicate zeolites [65]. In contrast, the smaller desorption peak at the lower temperature (425 °C) of S17-K suggests that K^+ ions stay in the *can* cage (cannot be removed by exchange) and cover the strong acid sites. The stronger acidity of S17-N compared to previously reported SAPO-17s [20,21,66] can be attributed to its higher silica content and abundant Si(4Al) species.

The crystal structures of S17-N and S17-K were further determined by the continuous rotation electron diffraction (cRED) technique to confirm the existence and location of small inorganic cations. Their 3D reciprocal lattices were reconstructed based on the continuous cRED data. All framework atoms, except a few missing C and H atoms belonging to OSDA, could be resolved using SHELXTL [67]. Their crystallographic details are presented in Table S2. Both S17-N and S17-K samples crystallize in the $P6_3/m$ space group (No.176), and contain two crystallographically distinct P (P2 and P1 with occupancy of 1.0 and 0.5) and Al (Al1 and Al2 with occupancies of 1.0 and 0.5) sites, respectively. The structure consists of face-shared small *can* cages and d6rs, as well as the *eri* cages, forming a typical ERI structure. As expected, K^+ or NH_4^+ cations remain in the *can* cages, respectively, and TMHDA locates in the *eri* cage, as illustrated in Fig. 2. The substitution amount of Si atoms and the content of guest molecules were determined by XRF, TG and elemental analyses. Combined with the crystallographic data, the final molecular formula of the two compounds was determined as $(C_{10}H_{26}N_2)_2(NH_4)_2[Al_{17.5}P_{11.5}Si_{7.0}O_{72}]$ and $(C_{10}H_{26}N_2)_2(K)_2[Al_{17.5}P_{11.5}Si_{7.0}O_{72}]$.

The chemical environment of S17-N was further investigated by solid-state NMR spectroscopy. As shown in Fig. 3(a), the ^{31}P MAS NMR spectrum shows two sharp signals at –26 and –32 ppm, corresponding to P2 and P1 sites (Fig. 2), respectively. The detection of a minor peak at –21 ppm suggests the increased complexity of the P environment due to the introduction of silicon and the presence of guest molecules [68]. The ^{29}Si MAS NMR spectrum exhibits two major signals at –91 and –95 ppm, accompanied by multiple weak peaks at

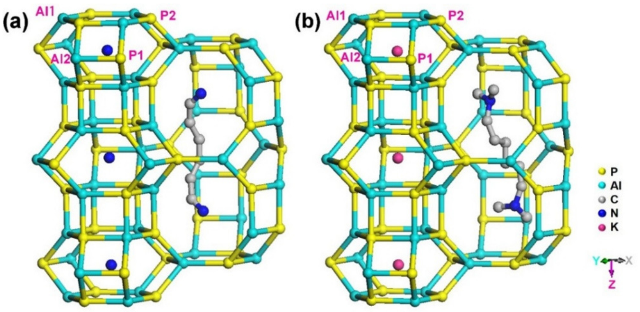

Fig. 2. The crystal structures of S17-N (a) and S17-K (b) viewed along the [110] direction. The positions of TMHDA (R) and inorganic cations are shown in it. Due to the high structural symmetry, the positioning of some methyl groups and H atoms failed.

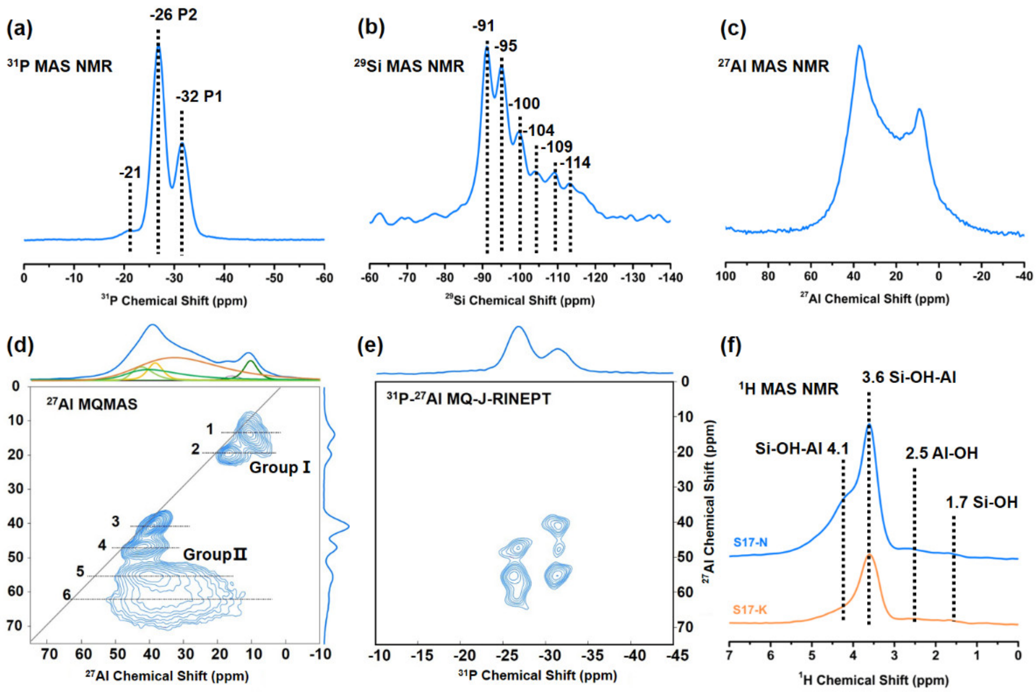

Fig. 3. Solid-state ^{31}P (a), ^{29}Si (b), ^{27}Al (c) MAS NMR, 2D ^{27}Al 3Q MAS NMR (d), 2D ^{31}P-^{27}Al MQ-J-RINEPT correlation MAS NMR (e) spectra of as-made S17-N. (f) ^{1}H MAS NMR spectra of calcined S17-N and S17-K.

–100, –104, -109, and –114 ppm (Fig. 3(b)). The first two peaks are supposed to be Si(4Al) species formed by the substitution of the two distinct P positions [68], while the other signals can be ascribed to the Si(3Al), Si(2Al), Si(1Al), and Si(0Al) species, accordingly, resulting from the complicated chemical environments. After calcination, the ^{29}Si MAS NMR spectrum merges into an asymmetric broad signal at approximately –90 ppm, with a minor shoulder peak at –109 ppm (Fig. S20). It forms a sharp contrast with that of conventional calcined S17-C (Fig. S13). The results confirm that the framework Si atoms exist mainly in the form of Si(4Al) with a limited amount of silicon island. The 1D ^{27}Al MAS NMR (Fig. 3(c)) spectrum of S17-N shows highly overlapped peaks with chemical shifts span from 0 to 50 ppm.The signals are further resolved to six distinct Al sites by the resolution-enhanced 2D ^{27}Al triple quantum (3Q) MAS NMR. As depicted in Figs. 3(d) and S21, the ^{27}Al NMR signals can be divided into two groups [69]. Group **I** comprises **1** and **2** two peaks at 10 and 17 ppm, respectively, which are attributed to five-fold coordinated Al signals likely bond to template TMHDA or water. They could be extra-framework alumina, since neither of them forms direct P-O-Al bond, as evidenced by the absence of the corresponding correlation signals in the ^{27}Al-^{31}P 3Q-*J*-refocused insensitive nuclei enhancement by polarization transfer (3Q-*J*-RINEPT, Fig. 3(e)) [70]. The other four signals (peaks **3**–**6**), which constitute Group **II**, are tetrahedrally coordinated framework Al signals. Among them, peaks **3** and **4** are related to the highly symmetric four-coordinated Al sites in $AlPO_4$ structures, as reflected by the narrow linewidth of peaks, and the high similarity to the ^{27}Al NMR signals of conventional AlPO-17 (Fig. S22). While the peaks **5** and **6** with higher isotropic chemical shifts exhibit evident quadrupolar broadening along the F2 dimension, indicating the increased asymmetry in the local environments of these Al sites, most likely due to the substitution of P atoms around Al by Si atoms. This is in consistence with the previous theoretical calculations that the second-order quadrupolar effect (SOQE) and chemical shifts of Al sites in aluminophosphate will increase with the introduction of Si atoms [71]. Notably, the evidently higher isotropic chemical shifts (50–70 ppm) and large quadrupolar coupling constants (C_{QS}, 6.2 and 7.0 MHz for peaks **5** and **6**) of these two Al sites are close to that of Al sites in many aluminosilicate zeolites [65,72–75], suggesting the potential local structural similarities between these Al sites and those of aluminosilicate. While the formation of these aluminosilicate-like local environment similar to that of zeolite tend to induce stronger acidity, which is further confirmed by the ^{1}H MAS NMR spectra (Fig. 3(f)). S17-N presents a characteristic Brønsted acid signal at 3.6 ppm with an additional peak at 4.1 ppm. The former is attributed to the characteristic Brønsted acid signal. The latter can be due to bridging hydroxyl groups [Si(OH)Al] from narrower structural units like *can* cage [76]. In contrast, S17-K and S17-C (Fig. S23) have weaker signals at 3.6 ppm. The shoulder peak at 4.1 ppm of S17-K is negligible. While, S17-C has a weak shoulder peak at 3.8 ppm due to the acidic site from *can* cage. The migration of chemical shift may be due to a poor silicon environment (Fig. S13). The findings are consistent with the NH_3-TPD results (Fig. S24), again demonstrating the stronger acidity of S17-N.

3.4. NH_3-SCR performance of Cu_x-SAPO-17s

The significantly increased acidity of S17-N encourages us to evaluate their $DeNO_x$ activity after copper-ions exchange. Fig. 4(a) shows the NO_x conversion as a function of reaction temperature over Cu_x-S17-N with different Cu^{2+} ion loadings (x = 1.6, 2.9 and 4.4). The subscript x represents the mass percentage of Cu atom. The NO_x conversion is 92% at 175 °C for fresh $Cu_{1.6}$-S17-N catalyst, which reaches 100% at 200 °C and remains at this level up to 650 °C at a gas hourly space velocity (GHSV) of 180000 h^{-1}. Its activity is still above 90% even at 700 °C. Such a broad temperature window ranging from 175–700 °C, with NO_x conversions exceeds 90% for the fresh catalyst (T_{90F}) has never been achieved before, as can be seen from the summary of the previously reported catalytic results in Table S3. The NO_x conversion at 175 °C enhances to 100% when the Cu loading is increased to 2.9 wt%, but the high temperature conversion above 90% shrinks to 650 °C. The excellent NH_3-SCR catalytic properties of $Cu_{2.9}$-S17-N are mostly maintained at an increased GHSV of 300000 h^{-1}, which are even superior to those of reported Cu-SSZ-13 (Fig. S25) [31,77]. When the Cu loading is increased to 4.4 wt%, the low-temperature activity cannot be further promoted even though the exchange degree of Cu^{2+} ions is about 80%. Meanwhile, the high temperature limit of T_{90F} has receded to 600 °C.

All the Cu_x-S17-Ns have robust hydrothermal stability. No severe activity degradation is observed after hydrothermal aging under 12% H_2O/air steaming at 750 °C for 16 h (Fig. 4(b)). The $Cu_{2.9}$-S17-N catalyst even survives more severe hydrothermal steaming treatments at 800 °C for 16 h. More importantly, $Cu_{2.9}$-S17-N catalyst exhibits excellent resistance to the low-temperature hydrothermal treatment at 80 °C for 24 h, as illustrated in Fig. 4(b). The N_2 selectivities over Cu_x-S17-Ns are all close to 100% (Fig. S26). The results demonstrate that Cu_x-S17-N is a promising catalyst candidate for NH_3-SCR reaction, capable of breaking the current bottleneck of the T_{90F} range about 200–550 °C.

3.5. Reasoning for the enhanced activity of Cu_x-S17-N

To understand the reason for the enhanced activity of Cu_x-S17-N, zeolites $Cu_{2.5}$-S17-K, $Cu_{2.8}$-S17-C, and $Cu_{2.5}$-ERI-6.4 (Fig. S27) with the same ERI topology and comparable Cu^{2+} ion loadings but different acidity (Figs. S24 and S28), were prepared to examine their catalytic performances as references. As shown in Fig. 4(c), the T_{90F} of $Cu_{2.5}$-S17-K, $Cu_{2.5}$-ERI-6.4 and $Cu_{2.8}$-S17-C were 175-550, 175-550, and 250-350 °C, respectively. After hydrothermal treatments at 750 °C for 16 h, the activities of $Cu_{2.8}$-S17-C and $Cu_{2.5}$-ERI-6.4 degraded dramatically (Fig. 4(d)), while $Cu_{2.5}$-S17-K maintained above 90% NO_x conversion from 250 to 500 °C. The inferior activity and durability of $Cu_{2.8}$-S17-C should be attributed to its uneven Si distribution (Fig. S13), resulting in weak acidity and poor Cu^{2+} ions dispersion. The degraded high-temperature activity and hydrothermal stability of $Cu_{2.5}$-S17-K and $Cu_{2.5}$-ERI-6.4 are attributable to the presence of K^+ ions [78–80]. In contrast, $Cu_{2.9}$-S17-N has a higher acid amount due to its high but uniform Si distribution and the absence of K^+ ions. It exposes more acidic sites to better stabilize the Cu^{2+} ion active sites. Meanwhile, the ability of NH_3 storage will be enhanced, weakening the side reaction of NH_3 oxidation [81]. Therefore, $Cu_{2.9}$-S17-N exhibits superior catalytic performance and hydrothermal stability due to the optimized acidity. On the other hand, the equally excellent low-temperature activity of fresh $Cu_{2.5}$-S17-K and $Cu_{2.5}$-ERI-6.4, along with that of $Cu_{2.9}$-S17-N, might suggest the advantages of the ERI structure for improving the low-temperature activity of NH_3-SCR.

The NH_3-SCR performance of $Cu_{3.0}$-S56-DMA synthesized by the SPDT method was also investigated as a reference with the similar acidity but different topology. As shown in Fig. S29, although the $Cu_{3.0}$-S56-DMA has a T_{90F} of 200–550 °C and a

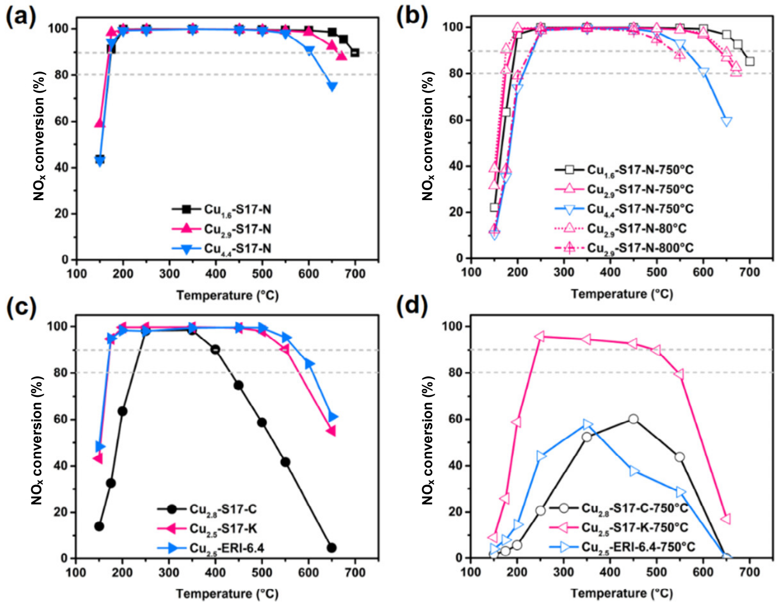

Fig. 4. NO_x conversions as a function of temperature during standard NH_3-SCR for fresh (a) and hydrothermal aged (b) Cu_x-S17-N, fresh (c) and hydrothermally aged (d) $Cu_{2.5}$-S17-K, $Cu_{2.8}$-S17-C and $Cu_{2.5}$-ERI-6.4 catalysts. Catalytic conditions: 500 ppm NO, 500 ppm NH_3, 14% O_2, 4.5% H_2O, balanced with N_2, GHSV = 180000 h^{-1}.

Table 2
Comparison of the structural characteristics and physical properties of molecular sieves.

Essential rings of three zeolite topologies [a]				
Structure type		ERI	CHA	AFX
Essential rings		[$8_1 \cdot 6_3 \cdot 4_2$]	[$8_1 \cdot 6_1 \cdot 4_2$]	[$8_2 \cdot 6_2 \cdot 4_4$]
The percentage of 6-ring units (%)		52.9	27.3	27.3
Deconvolution results of the distributions of paired acidic sites [b]				
Sample	Paired acidic sites (%)	τ (%)	ω (%)	σ (%)
Co-S17-N	77.8	32.8	38.8	6.1
Co-ERI-6.4	26.0	9.1	15.3	1.6

[a] The percentage of 6-ring units is calculated by the number of atoms in 6-rings/the sum of atoms in essential rings. [b] Deconvoluted results of DR UV-vis spectra of dehydrated Co-exchanged zeolites.

superior hydrothermal stability compared to conventional SAPO-56 [57], its activity window is still narrower than that of $Cu_{2.9}$-S17-N. Since $Cu_{3.0}$-S56-DMA has comparable high Si content and more Si(4Al) species, the insufficient activity at both low and high temperature regions should be ascribed to the feature of zeolite structure. Essential ring is a descriptor which is more suitable and simple for characterizing a framework and its channels [63,82]. The number of each ring size is given by it. A comparison of the essential rings of ERI [$8_1 \cdot 6_3 \cdot 4_2$], CHA [$8_1 \cdot 6_1 \cdot 4_2$] and AFX [$8_2 \cdot 6_2 \cdot 4_4$] revealed that ERI has the highest 6-ring unit content (Table 2), which might be one of the reasons for its impressive NH_3-SCR activity [42].

H_2-TPR measurements (Fig. 5(a)) were performed to investigate the reducibility and chemical states of Cu species of Cu_x-S17-N. $Cu_{1.6}$-S17-N has only a reduction peak at 305 °C ascribed to the reduction of isolated Cu^{2+} to Cu^+ ions [46]. As the Cu loading increases to 2.9%, the main H_2 consumption peak gets strong and moves to 268 °C. It indicates that the Cu^{2+} ions of Cu-SAPO-17 catalyst get easier to be reduced as the increased copper content [83]. The H_2-TPR profile of $Cu_{2.9}$-S17-N also has another small H_2 consumption peak at 389 °C. It should be attributed to the reduction of Cu^{2+}-2Z next to the 6-ring [46,81,84]. For $Cu_{4.4}$-S17-N, the reduction peak of 268 °C gets widened, and another peak at 623 °C appears. The high-temperature reduction peak can be attributed to the reduction of Cu^+ to Cu^0 [85,86]. The H_2-TPR results confirm again that the optimal Cu loading amount of S17-N should be around 3.0%.

EPR measurements were further conducted to investigate the status of Cu species of $Cu_{2.9}$-S17-N before and after hydrothermal treatments at both high and low temperatures. As shown in Fig. 5(b) and Table S4, all of the samples have more than 60% isolated Cu^{2+} ions, confirming the excellent hydrothermal stability. Similarly, their UV-vis spectra (Fig. S30) show characteristic bands at 200–250 and 600–800 nm due to the charge transfer of lattice oxygen to isolated Cu^+/Cu^{2+} ions ($O^{2-} \rightarrow Cu^{2+}$ transition) and *d-d* transition bond of Cu^{2+} in the octahedral environment, respectively [46]. The absence of adsorption bands in the range of 350-400 nm again indicates the robust of $Cu_{2.9}$-S17-N catalysts.

To explore the oxidation state and local structure of Cu species at the atomic level, X-ray absorption spectroscopy (XAS) was utilized. Fig. 5(c) illustrates the Cu K-edge XANES for $Cu_{2.9}$-S17-N and $Cu_{2.9}$-S17-N-HT, with Cu foil, CuO, and Cu_2O serving as references. The oxidation state of Cu in both samples should be +2, as their white line intensities are similar to the CuO reference [87]. The local structure of Cu species in $Cu_{2.9}$-S17-N and $Cu_{2.9}$-S17-N-HT was obtained through analyzing the EXAFS spectra, as illustrated in Fig. 5(d), Table S5 and Fig. S31. The k^2-weighted EXAFS spectra of the Cu *K*-edge for $Cu_{2.9}$-S17-N and $Cu_{2.9}$-S17-N-HT in the R space exhibit similar scatterings at approximately 1.5 Å (uncorrected distance), which are assigned to the first shell of Cu-O with coordination number of 4 [88]. For the $Cu_{2.9}$-S17-N sample, no path can be

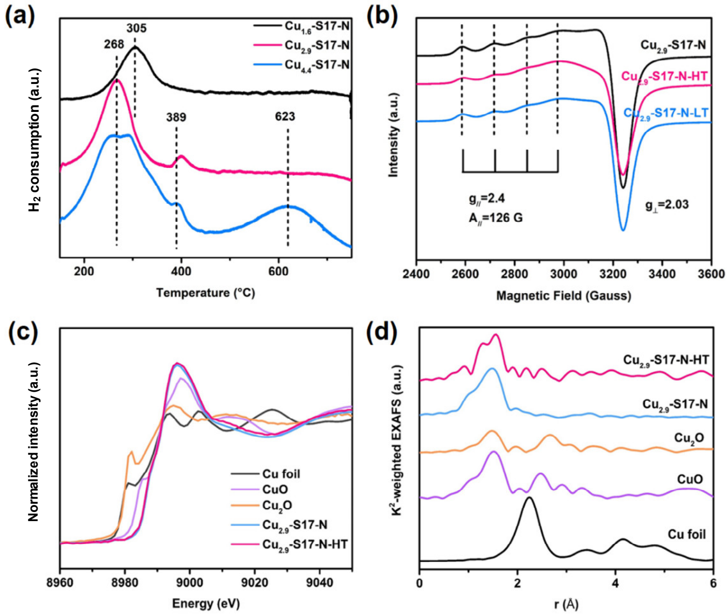

Fig. 5. (a) H_2-TPR curves of fresh $Cu_{1.6}$-S17-N, $Cu_{2.9}$-S17-N and $Cu_{4.4}$-S17-N. (b) EPR spectra of fresh and hydrothermally aged $Cu_{2.9}$-S17-N. (c) XANES spectra of $Cu_{2.9}$-S17-N, $Cu_{2.9}$-S17-N-HT and reference materials. (d) EXAFS of Cu K-edge of $Cu_{2.9}$-S17-N, $Cu_{2.9}$-S17-N-HT and reference materials (not corrected for phase shift).

fitted at a longer distance, suggesting Cu single sites were formed. However, a Cu-O-Cu path with a coordination number of 0.4±0.3 was highly needed to obtain a reasonable fit (reasonable σ^2 and R factor) in the $Cu_{2.9}$-S17-N-HT sample. This is an indicator that a small amount of Cu_nO_x clusters were formed under hydrothermal conditions. These results are consistent with the observations obtained through the TEM and HAADF-STEM (Fig. S32). There is no discernible particles on the surface of the fresh $Cu_{2.9}$-S17-N catalyst, whereas only a very small amount of particles were observed on the surface of the hydrothermally aged $Cu_{2.9}$-S17-N-HT sample.

Acidic pairing sites are considered a desired distribution for stabilize Cu^{2+} ions and enhancing the catalyst stability [89]. Conventionally, there are three types of possible adjacent cationic sites formed by neighbouring Al atoms (Al pairs) in the SSZ-13 framework [90]. They are σ site in the 6-ring, ω site inside the hexagonal prism of the d6r, and the τ site in the 8-ring. Similar to CHA, the ERI structure belongs to the ABC-6 family and is featured by the 6-ring stacking sequence of AABAAC layers. The S17-N with ERI topology, high silica content and uniform Si distribution should have abundant linkages of Si–O–Al–O–P–O–Al–O–Si and Si–O–Al–O–Si with similar function of Al pairs in SSZ-13. For S17-N, the possible paired acidic sites are shown in Fig. 6 including the σ, ω and τ Sites of I-VI. Their amounts were estimated through Co(II) cations as probes and monitored by UV-vis spectroscopy. As shown in Fig. S33 and Table 2, the paired acidic sites of Co-S17-N account for 77.8% of the total Si content versus 26% for the reference sample Co-ERI-6.4. The τ and ω sites of Co-S17-N are relatively more, accounting for 32.8% and 38.8%, respectively. It should be noted that the 20% Si content of S17-N is quite high, and the acid density is comparable to that of zeolite with Si/Al of 4. Thus, the absolute amounts of τ and ω sites are also very high. It indicates that the paired acid sites located in d6rs and 8-rings are more abundant, favoring the stabilization of isolated Cu^{2+} ions.

According to previous reports, $[Cu(OH)]^+$-Z and Cu^{2+}-2Z are the two active centers of molecular sieve catalysts [23–25,91,92]. The former normally stays in 8-rings, which has higher mobility as the main active species in the low temperature range (≤ 350 °C). The mobility of the Cu complex was recently revealed to be strongly dependent on the spatial distribution features of the framework Brønsted acid sites [26]. The increased acidity of S17-N together with its larger 8-ring size and window area (5.1 × 3.6 Å^2) than AFX (3.6 × 3.4 Å^2) and CHA (3.8 × 3.8 Å^2) have positive effects on its low-temperature NH_3-SCR performance. Cu^{2+}-2Z, which usually appears more in 6-rings, has stronger interaction with molecular sieve skeleton, and is responsible for high-temperature activity and hydrothermal stability. The increased content of ω and σ sites of Cu_x-S17-N explains its excellent high-temperature activity and hydrothermal stability. Cu_x-S17-Ns present as a potential NH_3-SCR catalyst with both wide active temperature window and excellent hydrothermal stability.

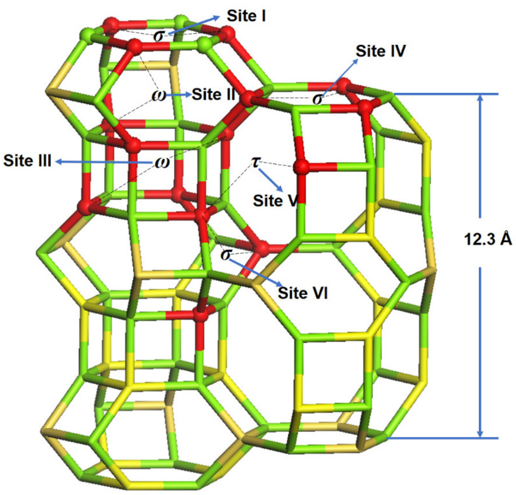

Fig. 6. The possible paired acidic sites and copper locations in the S17-N with ERI topology.

4. Conclusions

A variety of SAPO materials with high silica content and strong acidity have been synthesized by using a SAPO precursor and dual structural directing agent (SDA, template) assistant strategy (SPDT). The SAPO precursor, serving as the sole inorganic source, provides a rich set of Si containing active structural units to regulate the crystallization kinetics and promote the Si incorporation in the SAPO products. Meanwhile, the crystalline phase of the product is oriented from the inorganic precursors and dual templates. Especially, the secondary template plays a crucial crystalline-phase selection role for zeolites with multiple cage structures. The prepared copper ion-exchanged materials, $Cu_{1.6}$-S17-N, exhibits an unexpectedly wide activity temperature window in the NH_3-SCR reaction with wide T_{90F} of 175–700 °C. This breakthrough is mainly attributed to the suitable ERI structure and improved acidity of SAPO-17, thanks to the use of SPDT synthetic method. This study not only provides an effective strategy for the synthesis of SAPO molecular sieves with increased acidity, but also opens up a new perspective for widening the active temperature window of the NH_3-SCR reaction. We hope that highly acidic SAPO materials will have more catalytic applications in the future.

Author contributions

All authors contributed to this work. All authors have given approval to the final version of the paper.

Declaration of competing interest

The authors declare no competing financial interest.

Acknowledgment

We acknowledge DESY (Hamburg, Germany), a member of the Helmholtz Association HGF, for the prevision of experimental facilities. Parts of this research were carried out at PETRA III. Beamtime was granted for the proposal I-20240852.

We would like to thank Dr. Edmund Welter for assistance in using beamline P65, and Dr. Qiyang Zhang and Dr. Dmitry E. Doronkin for measurements. We also thank Prof. Dr. Peng Guo for cRED measurements and Prof. Dr. Shutao Xu for solid-state ^{1}H MAS NMR characterizations.

Electronic supporting information

Supporting information is available in the online version of this article.

References

[1] B. M. Lok, C. A. Messina, R. L. Patton, R. T. Gajek, T. R. Cannan, E. M. Flanigen, *J. Am. Chem. Soc.*, **1984**, 106, 6092–6093.

[2] P. Tian, Y. Wei, M. Ye, Z. Liu, *ACS Catal.*, **2015**, 5, 1922–1938.

[3] M. Yang, D. Fan, Y. Wei, P. Tian, Z. Liu, *Adv. Mater.*, **2019**, 31, 1902181.

[4] N. Katada, K. Nouno, J. K. Lee, J. Shin, S. B. Hong, M. Niwa, *J. Phys. Chem. C*, **2011**, 115, 22505–22513.

[5] H. Zhao, S. Shi, J. Wu, Y. Ding, N. Li, *Chin. J. Catal.*, **2016**, 37, 227–233.

[6] C. S. Blackwell, R. L. Patton, *J. Phys. Chem.*, **1988**, 92, 3965–3970.

[7] G. Sastre, D. W. Lewis, C. R. A. Catlow, *J. Mol. Catal. A*, **1997**, 119, 349–356.

[8] Z. Liu, *Methanol to Olefins*, Beijing: Science Press, **2015**, 133.

[9] D. Barthomeuf, *Zeolites*, **1994**, 14, 394–401.

[10] G. Sastre, D. W. Lewis, *Faraday Trans.*, **1998**, 94, 3049–3058.

[11] G. A. V. Martins, G. Berlier, S. Coluccia, H. O. Pastore, G. B. Superti, G. Gatti, L. Marchese, *J. Phys. Chem. C*, **2007**, 111, 330–339.

[12] P. Tian, X. Su, Y. Wang, Q. Xia, Y. Zhang, D. Fan, S. Meng, Z. Liu, *Chem. Mater.*, **2011**, 23, 1406–1413.

[13] X. Su, P. Tian, D. Fan, Q. Xia, Y. Yang, S. Xu, L. Zhang, Y. Zhang, D. Wang, Z. Liu, *ChemSusChem*, **2013**, 6, 911–918.

[14] X. Su, S. Xu, P. Tian, J. Li, A. Zheng, Q. Wang, M. Yang, Y. Wei, F. Deng, Z. Liu, *J. Phys. Chem. C*, **2015**, 119, 2589–2596.

[15] F. H. Alshafei, Y. Park, S. I. Zones, M. E. Davis, *J. Catal.*, **2021**, 404, 620–633.

[16] A. Tuel, C. Lorentz, V. Gramlich, C. Baerlocher, *Comptes Rendus Chim.*, **2005**, 8, 531–540.

[17] P. Feng, X. Bu, C.-S. Yang, *Microporous Mesoporous Mater.*, **2001**, 50, 145–149.

[18] S. Han, W. Rao, J. Hu, X. Tang, Y. Ma, J. Du, Z. Liu, Q. Wu, Y. Ma, X. Meng, W. Shan, F.-S. Xiao, H. He, *Appl. Catal. B*, **2023**, 332, 122746.

[19] F. H. Alshafei, J. H. Kang, S. J. Cho, M. E. Davis, *Inorg. Chem.*, **2023**, 62, 6065–6075.

[20] Z. Duan, N. Wang, H. Xu, P. Wu, *Inorg. Chem.*, **2022**, 61, 8066–8075.

[21] X. Liu, Y. Cao, N. Yan, C. Ma, L. Cao, P. Guo, P. Tian, Z. Liu, *Chin. J. Catal.*, **2020**, 41, 1715–1722.

[22] D. Wang, M. Yang, W. Zhang, D. Fan, P. Tian, Z. Liu, *CrystEngComm*, **2016**, 18, 1000–1008.

[23] M. Iwamoto, H. Furukawa, Y. Mine, F. Uemura, S.-I. Mikuriya, S. Kagawa, *J. Chem. Soc., Chem. Commun.*, **1986**, 1272–1273.

[24] S. T. Korhonen, D. W. Fickel, R. F. Lobo, B. M. Weckhuysen, A. M. Beale, *Chem. Commun.*, **2011**, 47, 800–802.

[25] E. Borfecchia, K. A. Lomachenko, F. Giordanino, H. Falsig, P. Beato, A. V. Soldatov, S. Bordiga, C. Lamberti, *Chem. Sci.*, **2015**, 6, 548–563.

[26] Y. Fu, W. Ding, H. Lei, Y. Sun, J. Du, Y. Yu, U. Simon, P. Chen, Y. Shan, G. He, H. He, *J. Am. Chem. Soc.*, **2024**, 146, 11141–11151.

[27] I. Heo, S. Sung, M. B. Park, T. S. Chang, Y. J. Kim, B. K. Cho, S. B. Hong, J. W. Choung, I.-S. Nam, *ACS Catal.*, **2019**, 9, 9800–9812.

[28] T. Selleri, I. Nova, E. Tronconi, V. Schmeisser, S. Seher, *Catal. Today*,

Graphical Abstract

Chin. J. Catal., 2025, 78: 279–291 doi: 10.1016/S1872-2067(25)64801-7

Precursor and dual-template assisted synthesis of highly acidic SAPO-17 molecular sieve: Excellent NH_3-SCR activity of Cu-exchanged forms

Ye Wang, Pan Gao, Dan Zhao, Tongrui Liu, Sitong Zhou, Miao Yang *, Shiping Liu, Bing Li, Yida Zhou, Wenhao Cui, Guangjin Hou, Peng Tian, Zhongmin Liu *
Zhengzhou University; Dalian Institute of Chemical Physics, Chinese Academy of Sciences

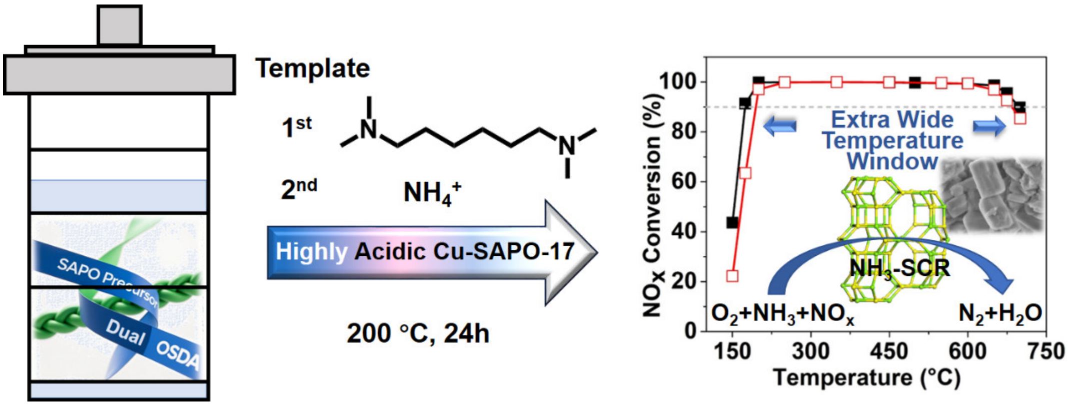

A SAPO precursor and dual template-assisted synthetic strategy (SPDT) was developed to synthesize SAPO materials with high acidity. The synthesized Cu-SAPO-17 exhibits unexpectedly wide active temperature window in the NH_3-SCR reaction thanks to its special ERI structure and increased acidity.

2019, 320, 100–111.

[29] Y. Zhang, Y. Peng, J. Li, K. Groden, J.-S. McEwen, E. D. Walter, Y. Chen, Y. Wang, F. Gao, *ACS Catal*., **2020**, 10, 9410–9419.

[30] A. M. Beale, I. Lezcano-Gonzalez, W. A. Slawinksi, D. S. Wragg, *Chem. Commun*., **2016**, 52, 6170–6173.

[31] J. H. Kwak, R. G. Tonkyn, D. H. Kim, J. Szanyi, C. H. F. Peden, *J. Catal*., **2010**, 275, 187–190.

[32] U. Deka, I. Lezcano-Gonzalez, B. M. Weckhuysen, A. M. Beale, *ACS Catal*., **2013**, 3, 413–427.

[33] J. Luo, F. Gao, K. Kamasamudram, N. Currier, C. H. F. Peden, A. Yezerets, *J. Catal*., **2017**, 348, 291–299.

[34] Q. Zhang, S. Gao, J. Yu, *Chem. Rev*., **2023**, 123, 6039–6106.

[35] Y. Shan, J. Du, Y. Zhang, W. Shan, X. Shi, Y. Yu, R. Zhang, X. Meng, F.-S. Xiao, H. He, *Natl. Sci. Rev*., **2021**, 8, nwab010.

[36] T. Andana, K. G. Rappé, F. Gao, J. Szanyi, X. Pereira-Hernandez, Y. Wang, *Appl. Catal. B*, **2021**, 291, 120054.

[37] F. Gao, J. Szanyi, *Appl. Catal. A*, **2018**, 560, 185–194.

[38] B. Ipek, M. J. Wulfers, H. Kim, F. Göltl, I. Hermans, J. P. Smith, K. S. Booksh, C. M. Brown, R. F. Lobo, *ACS Catal*., **2017**, 7, 4291–4303.

[39] B. Chen, J. Cheng, J. Qiao, C. Dai, R. Xu, G. Yu, N. Wang, J. Xing, N. Liu, *Fuel*, **2023**, 348, 128501.

[40] J. Zhu, Z. Liu, L. Xu, T. Ohnishi, Y. Yanaba, M. Ogura, T. Wakihara, T. Okubo, *J. Catal*., **2020**, 391, 346–356.

[41] J. Zhu, Z. Liu, K. Iyoki, C. Anand, K. Yoshida, Y. Sasaki, S. Sukenaga, M. Ando, H. Shibata, T. Okubo, T. Wakihara, *Chem. Commun*., **2017**, 53, 6796–6799.

[42] T. Ryu, N. H. Ahn, S. Seo, J. Cho, H. Kim, D. Jo, G. T. Park, P. S. Kim, C. H. Kim, E. L. Bruce, P. A. Wright, I.-S. Nam, S. B. Hong, *Angew. Chem. Int. Ed*., **2017**, 56, 3256–3260.

[43] J. Lin, K. Lee, S. B. Hong, *Catal. Today*, **2021**, 376, 41–46.

[44] D. Jo, T. Ryu, G. T. Park, P. S. Kim, C. H. Kim, I.-S. Nam, S. B. Hong, *ACS Catal*., **2016**, 6, 2443–2447.

[45] R. G. Chitac, J. Bradley, N. D. McNamara, A. Mayoral, A. Turrina, P. A. Wright, *Chem. Mater*., **2021**, 33, 5242–5256.

[46] Y. Wang, J. Han, M. Chen, W. Lv, P. Meng, W. Gao, X. Meng, W. Fan, J. Xu, W. Yan, J. Yu, *Angew. Chem. Int. Ed*., **2023**, 62, e202306174.

[47] J. Han, J. Li, W. Zhao, L. Li, M. Chen, X. Ge, S. Wang, Q. Liu, D. Mei, J. Yu, *J. Am. Chem. Soc*., **2024**, 146, 7605–7615.

[48] X. Xiang, M. Yang, B. Gao, Y. Qiao, P. Tian, S. Xu, Z. Liu, *RSC Adv*., **2016**, 6, 12544–12552.

[49] Y. Cao, D. Fan, P. Tian, L. Cao, T. Sun, S. Xu, M. Yang, Z. Liu, *Chem. Eng. J*., **2018**, 354, 85–92.

[50] Y. Cao, D. Fan, L. Sun, M. Yang, L. Cao, T. Sun, S. Xu, P. Tian, Z. Liu, *Chem. Eng. J*., **2019**, 374, 832–839.

[51] L. Sun, M. Yang, L. Cao, Y. Cao, S. Xu, D. Zhu, P. Tian, Z. Liu, *Microporous Mesoporous Mater*., **2020**, 309, 110585.

[52] J. Hou, C. Yin, C. Zhong, L. Wang, R. Wang, Z. Zhao, M. Ke, *Ind. Eng. Chem. Res*., **2022**, 61, 15169–15180.

[53] L. Sun, M. Yang, Y. Cao, P. Tian, P. Wu, L. Cao, S. Xu, S. Zeng, Z. Liu, *Chin. J. Catal*., **2020**, 41, 1410–1420.

[54] T. Yu, D. Fan, T. Hao, J. Wang, M. Shen, W. Li, *Chem. Eng. J*., **2014**, 243, 159–168.

[55] A. Wang, Y. Chen, E. D. Walter, N. M. Washton, D. Mei, T. Varga, Y. Wang, J. Szanyi, Y. Wang, C. H. F. Peden, F. Gao, *Nat. Commun*., **2019**, 10, 1137.

[56] G. Liu, P. Tian, Y. Zhang, J. Li, L. Xu, S. Meng, Z. Liu, *Microporous Mesoporous Mater*., **2008**, 114, 416–423.

[57] L. Xu, Y. Wang, Y. Cao, F. Zhang, Y. Song, C. Yu, P. Tian, L. Sun, *Microporous Mesoporous Mater*., **2024**, 366, 112978.

[58] Y. Tang, Q. Wang, N. Yan, X. Zhang, M. Yang, P. Tian, Z. Liu, *Chem. Res. Chin. Univ*., **2024**, 40, 1171–1178.

[59] J. P. Amoureux, C. Fernandez, *Solid State Nucl. Magn. Reson*., **1998**, 10, 211–223.

[60] D. Massiot, F. Fayon, M. Capron, I. King, S. Le Calvé, B. Alonso, J.-O. Durand, B. Bujoli, Z. Gan, G. Hoatson, *Magn. Reson. Chem*., **2002**, 40, 70–76.

[61] B. Ravel, M. Newville, *J. Synchrotron Radiat*., **2005**, 12, 537–541.

[62] X. Zhang, M. Yang, L. Wang, J. Han, C. Lou, S. Xu, Y. Zhang, R.-A. Wu, P. Tian, Z. Liu, *Chem. Eur. J*., **2023**, 29, e202203886.

[63] http://www.iza-structure.org/databases/.

[64] Y. Naraki, K. Ariga, K. Nakamura, K. Okushita, T. Sano, *Microporous Mesoporous Mater*., **2017**, 254, 160–169.

[65] J. Zhu, K. Muraoka, T. Ohnishi, Y. Yanaba, M. Ogura, A. Nakayama, T. Wakihara, Z. Liu, T. Okubo, *Adv. Sci*., **2024**, 11, 2307674.

[66] S. Zhong, S. Song, B. Wang, N. Bu, X. Ding, R. Zhou, W. Jin, *Microporous Mesoporous Mater*., **2018**, 263, 11–20.

[67] G. M. Sheldrick, *Acta Crystallogr. A,* **2015**, 71, 3–8.

[68] B. Zibrowius, U. Lohse, *Solid State Nucl. Magn. Reson*., **1992**, 1, 137–148.

[69] L. Frydman, J. S. Harwood, *J. Am. Chem. Soc*., **1995**, 117, 5367–5368.

[70] J. W. Wiench, M. Pruski, *Solid State Nucl. Magn. Reson*., **2004**, 26, 51–55.

[71] H. Koller, E. L. Meijer, R. A. van Santen, *Solid State Nucl. Magn. Reson*., **1997**, 9, 165–175.

[72] K. Chen, S. Horstmeier, V. T. Nguyen, B. Wang, S. P. Crossley, T. Pham, Z. Gan, I. Hung, J. L. White, *J. Am. Chem. Soc*., **2020**, 142, 7514–7523.

[73] K. Chen, Z. Gan, S. Horstmeier, J. L. White, *J. Am. Chem. Soc*., **2021**, 143, 6669–6680.

[74] B. Fan, D. Zhu, L. Wang, S. Xu, Y. Wei, Z. Liu, *Inorg. Chem. Front*., **2022**, 9, 3609–3618.

[75] B. Fan, W. Zhang, P. Gao, G. Hou, R. Liu, S. Xu, Y. Wei, Z. Liu, *J. Phys. Chem. Lett*., **2022**, 13, 5186–5194.

[76] A. Buchholz, W. Wang, M. Xu, A. Arnold, M. Hunger, *J. Phys. Chem. B*, **2004**, 108, 3107–3113.

[77] T. Liu, L. Wang, L. He, H. Chen, D. Fan, D. Zhu, M. Yang, P. Tian, Z. Liu, *Chem. Eng. J*., **2025**, 514, 163003.

[78] L. Wang, W. Li, S. J. Schmieg, D. Weng, *J. Catal*., **2015**, 324, 98–106.

[79] C. Fan, Z. Chen, L. Pang, S. Ming, C. Dong, K. Brou Albert, P. Liu, J. Wang, D. Zhu, H. Chen, T. Li, *Chem. Eng. J*., **2018**, 334, 344–354.

[80] S. Cimino, G. Totarella, M. Tortorelli, L. Lisi, *Chem. Eng. J*., **2017**, 330, 92–101.

[81] J. Song, Y. Wang, E. D. Walter, N. M. Washton, D. Mei, L. Kovarik, M. H. Engelhard, S. Prodinger, Y. Wang, C. H. F. Peden, F. Gao, *ACS Catal*., **2017**, 7, 8214–8227.

[82] O. Delgado Friedrichs, M. O'Keeffe, O. M. Yaghi, *Acta Cryst*., **2003**, A59, 22–27.

[83] J. He, D. Mao, J. Hou, C. Zhong, C. Yin, Z. Zhao, R. T. Yang, *Fuel*, **2023**, 339, 126927.

[84] Y. Shan, W. Shan, X. Shi, J. Du, Y. Yu, H. He, *Appl. Catal. B*, **2020**, 264, 118511.

[85] J. Du, Y. Shan, Y. Sun, M. Gao, Z. Liu, X. Shi, Y. Yu, H. He, *Appl. Catal. B*, **2021**, 294, 120237.

[86] R. Yu, Z. Zhao, S. Huang, W. Zhang, *Appl. Catal. B*, **2020**, 269, 118825.

[87] X. Tang, L. Wang, B. Yang, C. Fei, T. Yao, W. Liu, Y. Lou, Q. Dai, Y. Cai, X.-M. Cao, W. Zhan, Y. Guo, X.-Q. Gong, Y. Guo, *Appl. Catal. B*, **2021**, 285, 119827.

[88] X. Han, M. Bian, K. Liu, X. Yang, Y. Zhang, *J. Hazard. Mater*., **2024**, 480, 136112.

[89] J. Lin, X. Hu, Y. Li, W. Shan, X. Tan, H. He, *Appl. Catal. B*, **2023**, 331, 122705.

[90] K. Mlekodaj, J. Dedecek, V. Pashkova, E. Tabor, P. Klein, M.

Urbanova, R. Karcz, P. Sazama, S. R. Whittleton, H. M. Thomas, A. V. Fishchuk, S. Sklenak, *J. Phys. Chem. C*, **2019**, 123, 7968–7987.

[91] H. Lee, I. Song, S. W. Jeon, D. H. Kim, *J. Phys. Chem. Lett.*, **2021**, 12, 3210–3216.

[92] C. Paolucci, A. A. Parekh, I. Khurana, J. R. Di Iorio, H. Li, J. D. Albarracin Caballero, A. J. Shih, T. Anggara, W. N. Delgass, J. T. Miller, F. H. Ribeiro, R. Gounder, W. F. Schneider, *J. Am. Chem. Soc.*, **2016**, 138, 6028–6048.

前驱体协同双模板剂辅助合成强酸性SAPO-17分子筛及其铜交换后优异的NH$_3$-SCR催化性能

王冶[a,b], 高攀[c], 赵丹[b], 刘桐睿[b], 周思彤[b], 杨淼[b,*], 刘世平[b], 李冰[b], 周易达[b],
崔文浩[d], 侯广进[c], 田鹏[b], 刘中民[b,*]

[a]郑州大学化学学院, 河南郑州450001
[b]中国科学院大连化学物理研究所, 洁净能源国家实验室, 低碳催化技术国家工程研究中心, 辽宁大连116023
[c]中国科学院大连化学物理研究所, 洁净能源国家实验室, 催化基础国家重点实验室, 辽宁大连116023
[d]中国科学院大连化学物理研究所, 能源研究技术平台, 辽宁大连116023

摘要: 磷酸硅铝(SAPO)分子筛因其丰富的拓扑结构和优异的水热稳定性, 在酸催化领域备受关注. 然而, 提升特定SAPO分子筛的酸性质仍面临巨大挑战, 使其难以应用于高酸性要求的催化反应. 与硅铝分子筛不同, SAPO分子筛的酸性质主要取决于磷酸铝骨架中的Si原子取代量和取代方式(形成不同的硅化学环境). 尽管已发展了多种新型模板剂和合成方法, 精准地协同调控SAPO材料的晶相、Si引入量和Si分布仍是研究者孜孜以求的目标.

本文发展了一种SAPO前驱体协同双模板剂(结构导向剂)辅助的合成新策略(SPDT), 实现了一系列强酸性SAPO分子筛, 包括SAPO-34/56共晶、SAPO-56和SAPO-17的合成. SAPO前驱体作为唯一的无机源为合成体系提供了丰富的富含Si−O−Al键的结构单元, 不仅调节结晶动力学还促进了Si原子的骨架引入. 第二模板剂同时起到晶相选择的作用. 在第一模板剂相同的合成体系中, 当不含第二模板剂时得到了SAPO-34/56共晶产物; 以二甲胺或三甲胺为第二模板剂时, 生成SAPO-56; 而引入氯化铵或氯化钾作为第二模板剂时则生成了高硅含量的SAPO-17分子筛. 利用积分差分相位衬度成像技术、二维固体核磁共振和连续旋转电子衍射等先进表征技术对合成的SAPO材料进行了详细表征. 值得关注的是, 基于SPDT策略制备的负载型Cu-SAPO-17分子筛(Cu$_{1.6}$-S17-N)在NH$_3$选择性催化还原(NH$_3$-SCR)反应中展现出超宽的活性温度窗口: 在180000 h^{-1}空速条件下, NO$_x$转化率90%以上的温度区间覆盖175–700 °C. 进一步的对比研究和表征显示Cu-SAPO-17优异的催化性能主要归因于SAPO-17独特的ERI结构和改善的酸性.

综上, 本文发展了一种强酸性SAPO分子筛的合成新策略, 实现了系列强酸性SAPO分子筛的合成. 基于该策略制备的SAPO-17分子筛在铜负载后展现出卓越的NH$_3$-SCR催化性能. 本工作不仅为合成高酸性SAPO分子筛提供了一种高效通用的策略, 还为SAPO材料在多相催化领域的应用开拓了更多可能; 同时也为拓展NH$_3$-SCR反应的活性温度窗口提供了全新的研究思路, 对基础研究与工业应用均具有重要意义.

关键词: SAPO分子筛; 氨选择性催化还原; 超宽活性温度窗口; Si分布; 酸性

收稿日期: 2025-06-03. 接受日期: 2025-08-05. 上网时间: 2025-11-05.

*通讯联系人. 电子信箱: yangmiao@dicp.ac.cn (杨淼), liuzm@dicp.ac.cn (刘中民).

基金来源: 国家重点研发计划(2024YFE0207000); 国家自然科学基金(22171259, 22288101); 中法国际研究框架(IRN)和榆林中科洁净能源创新研究院人工智能科技专项资助(DNL-YL A202206).